Scilight

Advanced Characterization

https://www.sciltp.com/journals/ac

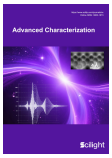

Review

Check for updates

Photoelectron Spectroscopy for Structural Characterization of Layered Transition Metal Dichalcogenides

Haoran Li [1,2], Hai Xu [1,*] and Liang Cao [2,*]

[1] Institutes of Physical Science and Information Technology, School of Optoelectronic Science and Engineering, Anhui University, Hefei 230601, China

[2] Anhui Provincial Key Laboratory of Low-Energy Quantum Materials and Devices, High Magnetic Field Laboratory, HFIPS, Chinese Academy of Sciences, Hefei 230031, China

* Correspondence: xuhai@ahu.edu.cn (H.X.); lcao@hmfl.ac.cn (L.C.)

How To Cite: Li, H.; Xu, H.; Cao, L. Photoelectron Spectroscopy for Structural Characterization of Layered Transition Metal Dichalcogenides. *Advanced Characterization* **2026**, *1*(1), 98–111. https://doi.org/10.53941/ac.2026.100008

Received: 1 May 2026

Revised: 24 June 2026

Accepted: 25 June 2026

Published: 30 June 2026

Abstract: Layered transition metal dichalcogenides (TMDs) exhibit remarkable structural flexibility and electronic tunability, where subtle structural variations, such as defects, self-intercalation, lattice distortion, stacking sequence and phase transitions, can significantly modify their physical properties. However, reliably identifying these structural degrees of freedom remains challenging when changes in stoichiometry or long-range order are minimal. Core-level photoelectron spectroscopy (PES) provides a uniquely sensitive approach to probe the local electronic structure and chemical environment. In this review, we establish a unified framework showing how different structural modulations give rise to distinct spectroscopic signatures governed by initial-state chemical shift and final-state core-hole screening. Vacancy defects and self-intercalation primarily induce core-level shifts of the defective element. Periodic lattice distortion leads to spectral splitting. Inter-layer sliding leads to subtle binding energy variations without new features. The structural phase transitions generate new spectral components with pronounced binding energy shifts. Using representative TMD systems, we demonstrate how core-level PES can identify defect types, quantify self-intercalation, clarify lattice distortion and track stacking arrangements and phase evolution. These capabilities highlight PES as a powerful probe of local structural modulation and many-body electronic responses, providing a direct spectroscopic link between structural variations and electronic properties.

Keywords: defect; self-intercalation; charge density wave; stacking order and structural phase transition

1. Introduction

The successful isolation of graphene has stimulated tremendous interest in layered materials [1]. Among them, transition metal dichalcogenides (TMDs), with the general formula MX_2 (where M denotes transition metals, and X chalcogen elements), have attracted extensive attention due to their rich physical properties and structural versatility [2,3]. These materials possess a layered structures characterized by strong intra-layer covalent bonding and weak inter-layer van der Waals (vdW) coupling. Such weak inter-layer coupling enables the scalable fabrication of large-area, high-quality atomic layer via mechanical exfoliation, chemical vapor deposition (CVD), and other synthetic techniques [4–6], thereby facilitating their integration into flexible electronics, integrated circuits, and next-generation devices.

Layered TMDs exhibit a wide range of electronic phases, including insulating, semiconducting, and metallic states, as well as correlated electronic states such as Mott-insulating states, charge density wave (CDW) and superconducting states [3,7]. This diversity gives rise to a broad spectrum of optical, electronic, magnetic, and thermal properties. This rich tunability underpins their broad applications in electronics, optoelectronics, spintronics, thermoelectrics, valleytronics, catalysis, and energy storage [2–5].

Despite their crystallinity, structural imperfections are inevitably present and play a crucial role in determining their device performance [8]. Therefore, reliable identification and characterization of such structural variations are essential for correctly interpreting experimental observations and for understanding the underlying physical mechanisms.

A variety of experimental techniques, including energy dispersive X-ray spectroscopy (EDX), Raman spectroscopy [9,10], X-ray diffraction (XRD) [10], scanning transmission electron microscopy (STEM) [10] and scanning probe microscopy (SPM) [10,11] have been widely employed to probe the structural characteristics of TMDs. These methods provide complementary information on composition, lattice structure, and morphology.

However, many subtle yet critical modifications, such as vacancy defects, self-intercalation, and structural transformations, often do not significantly alter the overall stoichiometry or long-range crystal structure, making them difficult to resolve using conventional techniques. Photoelectron spectroscopy (PES), in contrast, is uniquely sensitive to the electronic structure. By probing core-level energies and spectral line shapes, PES enables the detection of structural defects and structural evolution even when the elemental composition remains nearly unchanged. As such, it provides direct spectroscopic fingerprints of vacancy defects, self-intercalation, and structural distortion and transformations, as illustrated in Figure 1.

Photoelectron spectroscopy is a broad family of techniques that includes not only core-level spectroscopy, such as X-ray photoelectron spectroscopy (XPS), but also valence-band photoemission, ultraviolet photoelectron spectroscopy (UPS), and angle-resolved photoemission spectroscopy (ARPES). Valence-band PES and ARPES provide direct information on the occupied electronic states, band dispersion, Fermi-level position, and many-body electronic structures in layered TMDs. These capabilities are particularly useful for correlating structural modulations with changes in the low-energy electronic structure [12,13]. Nevertheless, the present review mainly focuses on core-level PES because core-level binding energies and line shapes are highly sensitive to the local chemical environment, coordination symmetry, charge redistribution, and core-hole screening response. Therefore, core-level PES provides a direct and element-specific spectroscopic fingerprint for identifying defects, self-intercalation, lattice distortion, stacking variations, and structural phase transitions in TMDs (cf. Figure 1).

In this review, we focus on PES studies of layered TMDs, with particular emphasis on its capability to reveal structural characteristics through distinct spectroscopic signatures. Section 2 introduces the fundamental principle of PES, including chemical shift and core-hole screening effects. Section 3 highlights representative applications identifying structural variations in TMDs. Finally, Section 4 provides a summary and outlook.

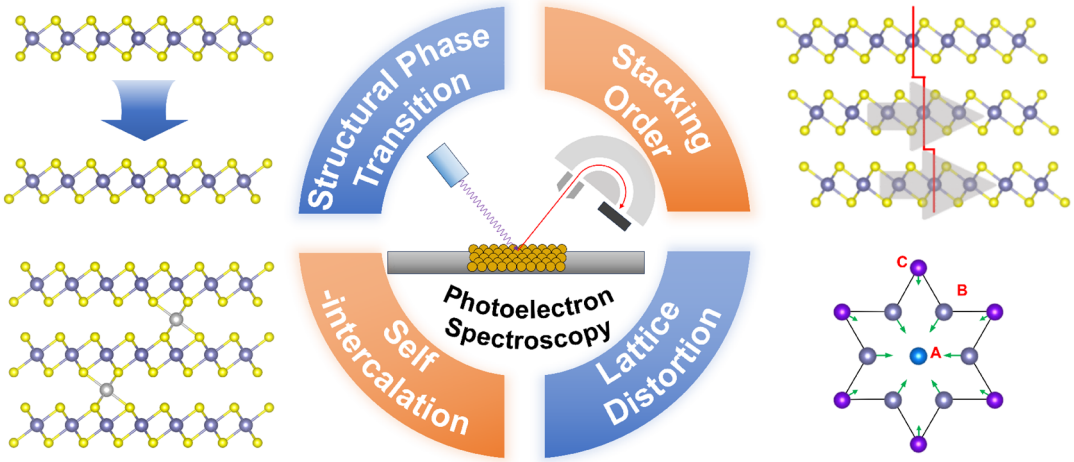

Figure 1. Schematic framework for identifying structural variations in layered TMDs using PES.

2. Fundamental Principle of PES

2.1. Basic Principles of PES

PES is based on the photoelectric effect. Figure 2 schematically illustrates the core-level photoemission process. In this process, a core-level electron is excited by incident photons with energy $h\nu$ exceeding its binding energies (E_B) and emitted as a photoelectron. Within the single-electron approximation, the kinetic energy (E_K) of the emitted electron is given by $E_K = h\nu - E_B - \varphi$, where E_B is the binding energy referenced to the Fermi level E_F, and φ is the work function of the materials. Each element possesses characteristic core-level binding energies, which serves as unique fingerprints for elemental identification. Consequently, PES is a powerful and widely used technique for determining the elemental composition of materials, including TMDs.

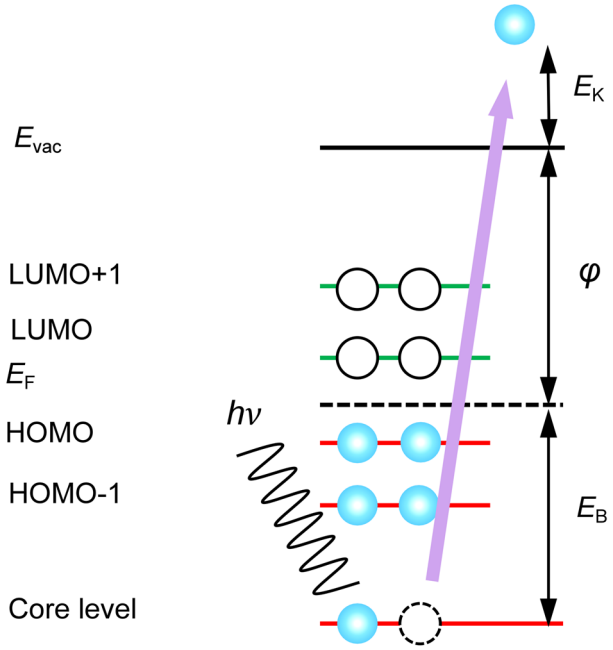

Figure 2. Schematic illustration of core-level photoemission.

2.2. Chemical Shift in PES

The binding energy of core-level electrons in PES is highly sensitive to the local chemical environment. Deviations from the binding energies of free atoms are referred to as chemical shift, which originate form initial-state effects associated with changes in the ground-state electronic structure.

The chemical environment is governed by factors including oxidation state, bonding configuration, electronegativity of neighboring atoms, and local coordination geometry. In general, an increase in oxidation states leads to an increasing of binding energy (cf. Figure 3). Similarly, bonding to atoms with a higher electronegativity enhances charge polarization, increasing the binding energy. For example, the C 1*s* binding energy for the C-O bonding configuration is larger than that of C-C, reflecting the strong electron-withdrawing effect of oxygen.

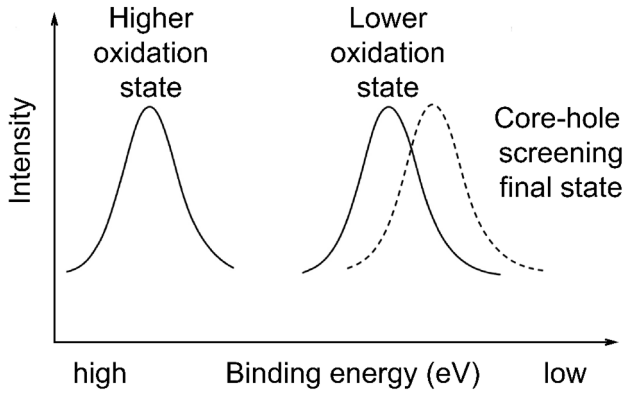

Figure 3. Schematic illustration of chemical shift and core-hole screening.

2.3. Core-Hole Screening Effect in PES

Beyond the single-electron approximation, photoemission is intrinsically a many-body process. The creation of a core-hole introduces a strong local potential, which induces a redistribution of the surrounding valence or conduction electrons to screen the core-hole potential (cf. Figure 4). This screening process lowers the total energy of the final state and gives rise to the final-state effects, significantly modifying the measured binding energies and spectral line shapes.

The efficiency of core-hole screening is strongly governed by the electronic structure. In metallic systems, in particular transition metals, the high density of states near the Fermi level enables rapid and efficient screening, often leading to asymmetric line shapes with characteristic high binding energy tail. In contrast, in semiconductors or insulators, reduced carrier mobility and electron localization results in inefficient screening, yielding more symmetric line shapes and weaker final-state effects. In strongly correlated systems, core-hole screening is often coupled with charge transfer processes, giving rise to multiplet splitting associated with different screening channels. In molecular system, intra-molecular polarization partially screens the core-hole potential, typically leading to the satellite features at higher binding energy.

It is important to emphasize that the experimental PES spectra are jointly determined by initial state effects (chemical shift) and final-state effects (core-hole screening). While changes in the chemical state primarily shift binding energies, variations in screening efficiency can further modulate the binding energy. More efficient screening general results in an additional shift towards lower binding energy, as illustrated in Figure 3 (guided by the dashed line). Structural variations, such as defects, self-intercalation, lattice distortion and phase transitions, can significantly modify the local electronic structure, carrier density, and hybridization strength, thereby altering the screening response. Consequently, the analysis of spectral features induced by chemical shifts and/or core-hole screening, particularly binding energy shifts, provides a sensitive and reliable approach to distinguish structural variations in TMDs.

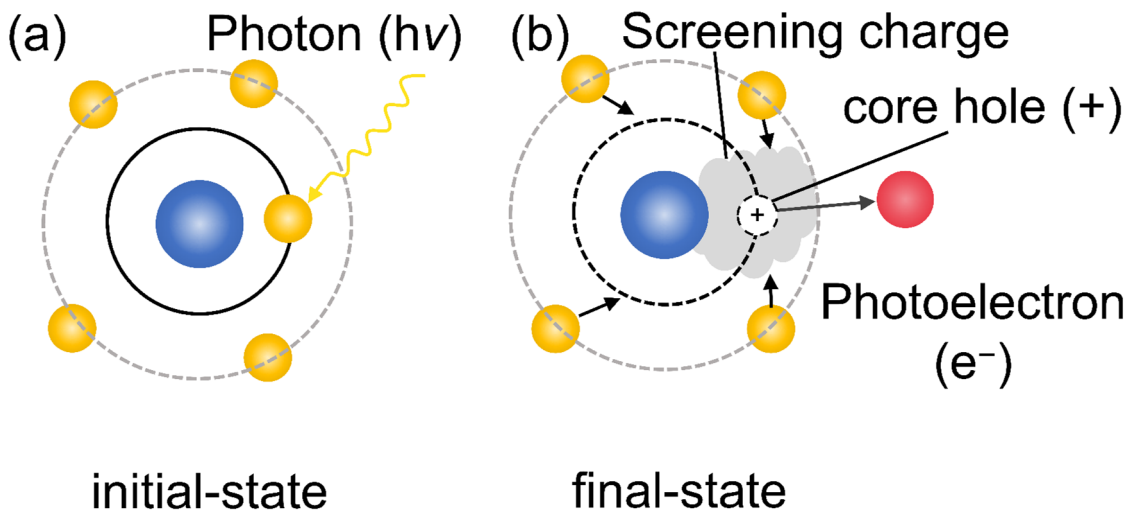

Figure 4. Schematic distinction between (**a**) initial-state and (**b**) final-state core-hole screening in PES.

Experimentally, PES measurement is commonly performed using laboratory X-ray sources such as Al-*K*α or Mg-*K*α, referred to as XPS, which are widely employed for probe of chemical states, chemical bonding in TMDs. Alternatively, synchrotron radiation provides tunable photon energies with high brilliance, enabling improved energy and spatial resolution. This is particularly important for two-dimensional TMDs, whereas subtle binding energy shifts encode detailed information on electronic structure and local structure.

3. Applications of PES Spectroscopy in Layered TMDs Characterization

Beyond overall stoichiometry, structural variations and subtle compositional variations play a central role in tuning the physical properties of layered TMDs. Among them, vacancies defects, self-intercalation and structural evolution represent three key mechanisms. Vacancies defects introduce localized states and modify carrier concentrations. Self-intercalation alters inter-layer coupling and injects additional charge carriers. Structural variation reconstructs lattice symmetry and orbital configurations. These effects critically influence the electronic structure and emergence of correlated phases.

Importantly, such subtle structural and compositional variations are often overlooked when interpreting the diverse physical properties reported for nominally identical TMDs, largely due to the limited sensitivity of conventional characterization techniques. For example, EDX, although widely used to determining elemental ratios, lacks sufficient sensitivity to the chemical bonding, making it difficult to distinguish lattice atoms from defect- or intercalation-related species.

As these effects primarily manifest in the electronic structure, particularly near the Fermi level, spectroscopic techniques with direct sensitivity to electronic structure are essential. In this context, PES, especially core-level spectra, provides a powerful approach to probe local chemical environment, and many-body interactions.

In the following section, we highlight representative applications of core-level PES in resolving these subtle yet crucial structural modifications in TMD materials.

3.1. Structural Defects

Structural defects are intrinsically generated in layered TMDs during material synthesis processes, such as chemical vapor transport (CVT), CVD and mechanical exfoliation. In addition, defects are deliberately introduced or further modified through post treatment processes, including thermal annealing and plasma exposure [14].

Depending on the targeted application, these defects can be either detrimental or beneficial. For instance, defect states often enhance catalytic activity by providing active sites, whereas they are generally undesirable in electronic and optoelectronic devices due to carrier scattering and performance degradation. Therefore, accurate identification and characterization of structural defects are essential for elucidating the underlying physico-chemical mechanisms and enabling the rational design of functional materials.

3.1.1. Vacancy Defects in 2H-WS_2

Atomic vacancies are among the most common structural defects in TMDs due to their relatively low formation energies, making them readily generated during synthesis or post-treatment processes. Such vacancies break local stoichiometric balance and induce electronic reconstruction, thereby modulating carrier density, mobility and optical response, as well as chemical activity and stability.

Figure 5a,b schematically illustrates the formation of S-vacancy on the surface of 2H-WS_2 crystals after Ar^+ bombardment. After sputtering, both W 4*f* and S 2*p* spectra exhibit noticeable broadening (Figure 5d–f), indicative of increased disorder. The generation of S-vacancies is directed evidenced by *in-situ* PES, as shown in Figure 5d,g. Compared with pristine 2H-WS_2, sputtering induced an additional low binding energy component in the W 4*f* spectrum, which is attributed to undercoordinated W-atoms in defective WS_{2-x}. This chemical shift reflects the increased local electron density at W-sites adjacent to S-vacancies. In contrast, no additional components are observed in the S 2*p* spectrum (Figure 5g), indicating that defect signature is primarily manifested on the W-sites.

The presence of S-vacancies, along with the absence of W-vacancies, is further supported by quantitative intensity analysis. The W 4*f* spectral intensity remains essentially unchanged after sputtering, whereas the S 2*p* intensity decreases significantly (Figure 5i), consistent with selective removal of S-atoms. Based on the extracted W:S ratio (Figure 5j), the S-vacancy concentration C_V^{exp} is yielded to be ~14%.

Upon air exposure, the overall intensities of both W 4*f* and S 2*p* spectra remain nearly constant, indicating that the elemental composition is preserved. However, the additional W 4*f* component shifts toward higher binding energy, while the S 2*p* spectrum remains largely unchanged (cf. Figure 5e,h). This behavior suggests the formation of WO_y species at S-vacancy sites due to the interaction with O_2/H_2O. The observed shift toward higher binding energy can be understood as a combined effect of chemical shift associated charge transfer to more electronegative O-atom and reduced core-hole screening associated with less conductive nature of WO_x, leading to poorly screened final state.

In addition to new features, a global binding energy shift of ~0.9 eV is observed for both W 4*f* and S 2*p* spectra (Figure 5d,g,e,h), indicating a downward shift of the Fermi level and the emergence of *p*-type-like doping. Notably, S-vacancies are unlikely to be the primary origin of this doping effect, as their filling does not restore the original binding energy positions (Figure 5e,h). Instead, a more plausible explanation is the incorporation of Ar^+ ions into the vdW gaps during sputtering, which can be further verified by subsequent gentle annealing.

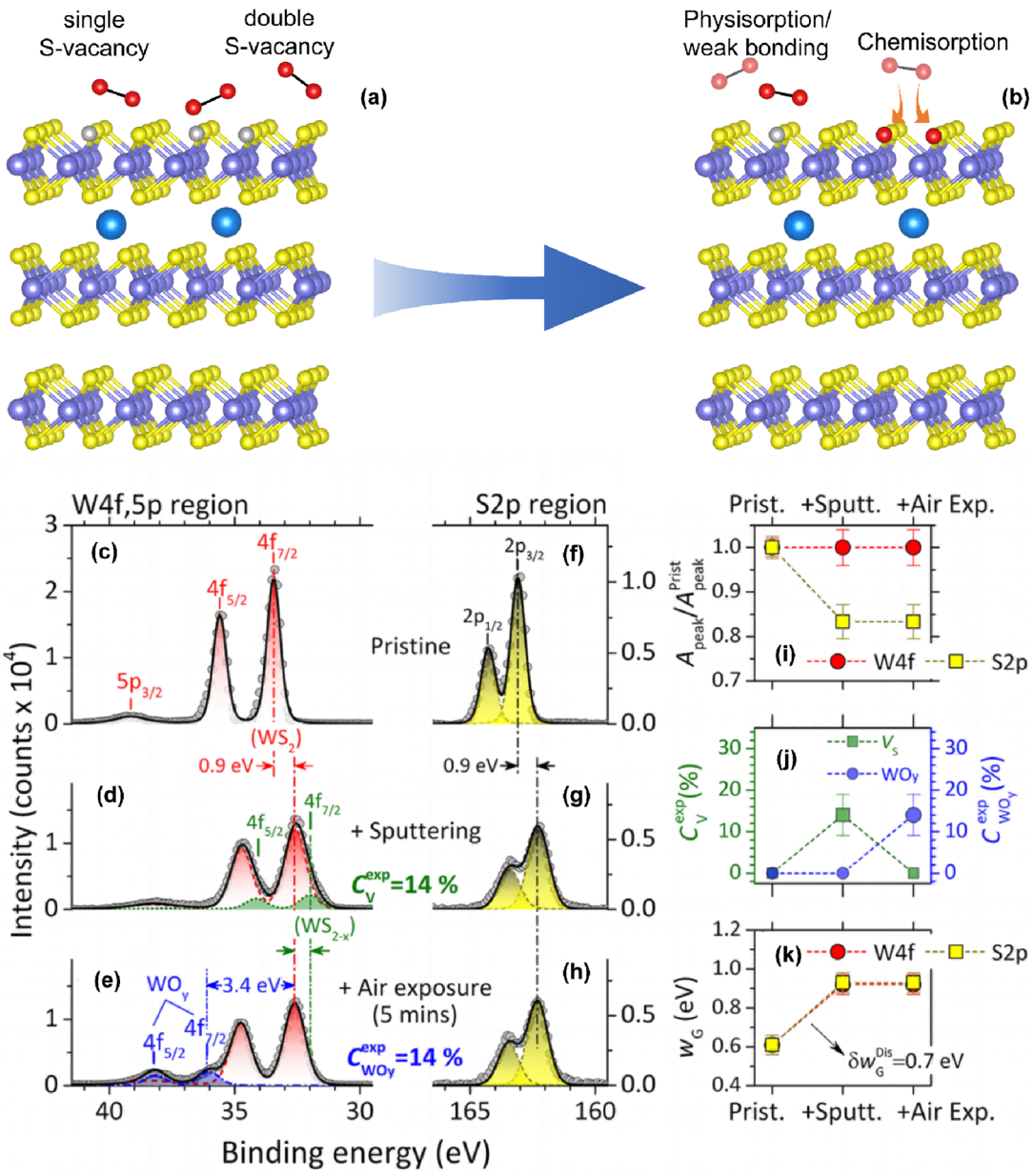

Figure 5. (**a**,**b**) Schematic illustration of 2H-WS_2 crystals and S-vacancies after Ar^+ ions sputtering, and the possible Ar^+ interted in vdW gap. The W 4*f* (**c**–**e**) and S 2*p* (**f**–**h**) core-level PES spectra for pristine 2H-WS_2 crystals, Ar^+ sputtering and subsequent 3 h air-exposure, respectively. The green shaded peaks in panel (**d**) and blue shaded peaks in panel (**e**) are attributed to S-vacancies associated WS_{2-x} and WO_y species, respectively. (**i**) The intensity ratio, (**j**) S-vacancy concentration C_V^{exp} and WO_y concentration $C_{WO_y}^{exp}$, and (**k**) Gaussian full width at half-maximum yielded from fitting [15]. Reproduced from Ref. [15] with permission. Copyright © 2024, American Chemical Society.

3.1.2. Self-Intercalation in 1T-TiS_2

Self-intercalation refers to the spontaneous incorporation of native host atoms into the vdW gaps of TMDs, forming interstitial-like species without introducing extrinsic impurities [16]. This phenomenon is particularly prevalent in TMDs systems with relatively weak inter-layer coupling, such as TaS_2 [17–19], NbS_2, $NbSe_2$ [20], $CrTe_2$ [21], TiS_2, $TiSe_2$ [22]. As an intrinsic defect engineering mechanism, self-intercalation provides an effective route to modulate material properties. The intercalated atoms act as charge reservoirs, inducing charge transfer that tunes the Fermi level, carrier density, and electron correlation strength. Meanwhile, the presence of intercalants modifies inter-layer coupling and stacking configurations, thereby influencing phase stability and even enabling emergent phenomena, such as charge density waves or superconductivity [18].

However, self-intercalation often introduces only subtle variations in stoichiometry and long-range structure, making it difficult to detect by conventional techniques. In this regard, the element-resolved PES serves as a

powerful and sensitive technique due to its sensitivity to the local chemical environment and electronic structure. In particular, self-intercalation can be identified and quantified through characteristic core-level shifts and/or spectral line-shape modifications associated with core-hole screening effects.

Figure 6a illustrate the crystal structure of 1T-TiS_2, highlighting Ti interstitials (Ti_i) in vdW gap, Ti Frenkel pair (Ti_F) and oxidation via S-vacancy filling. Figure 6b,c display the Ti $2p_{3/2}$ and S $2p$ core-level spectra of four as-growth 1T-TiS_2 crystals, respectively[23]. The asymmetrical spectral profile implies the presence of additional species beyond the stoichiometric TiS_2 host. In addition to the dominant features at ~456.2 eV (Ti^{4+}) and ~160.8 (S^{2-}), additional components (gray shaded peaks) appear at lower binding energy.

The possibility of S-vacancies can be ruled out, as they would primarily induce a single low binding energy shoulder in the Ti $2p$ spectrum. Instead, the observed features are attributed to self-intercalated Ti_i atoms residing in the vdW gap, forming Ti-S-Ti_i-S-Ti configurations. The incorporation of Ti_i leads to electron donation to the TiS_2 lattice, increasing the local electron density surrounding the neighboring atoms. This enhanced core-hole screening during the photoemission process, thereby reducing the effective core-hole potential and resulting in lower binding energy nature of Ti-S-Ti_i-S-Ti. From a many-body perspective, these spectral features directly reflect screening channels in which the core-hole is efficiently screened by excess electrons introduced by Ti_i. Conversely, oxidation also contributes a higher binding energy component observed in Ti $2p$ spectrum of one sample due to chemical shift associated with electron density withdrawn from Ti-atoms bonding to electronegativity of oxygen, and reduced core-hole screening.

Quantitative analysis can be performed by integrating the spectral weight of the decomposed c components. The Ti:S ratio derived from the dominant Ti^{4+} and S^{2-} peaks remains close to the stoichiometric value of 1:2, confirming the integrity of the host lattice. In contrast, the ratio extracted from the lower binding energy components approaches ~3:4, consistent with the Ti-S-Ti_i-S-Ti configuration. Accordingly, the nominal concentration of intercalated Ti_i can be estimated from the relative intensity ratio between Ti^{4+} and Ti–Ti_i–Ti components, as summarized in the molecular formula in Figure 6. The electron donation associated with Ti self-intercalation accounts for the elevated carrier concentration in TiS_2, which is particularly relevant for its thermoelectric performance.

Overall, self-intercalation and its impact on physical properties can be reliably monitored by PES through a self-consistent analysis of core-level shifts, spectral line shapes, and core-hole screening effects, enabling both qualitative identification and quantitative evaluation of intercalated species.

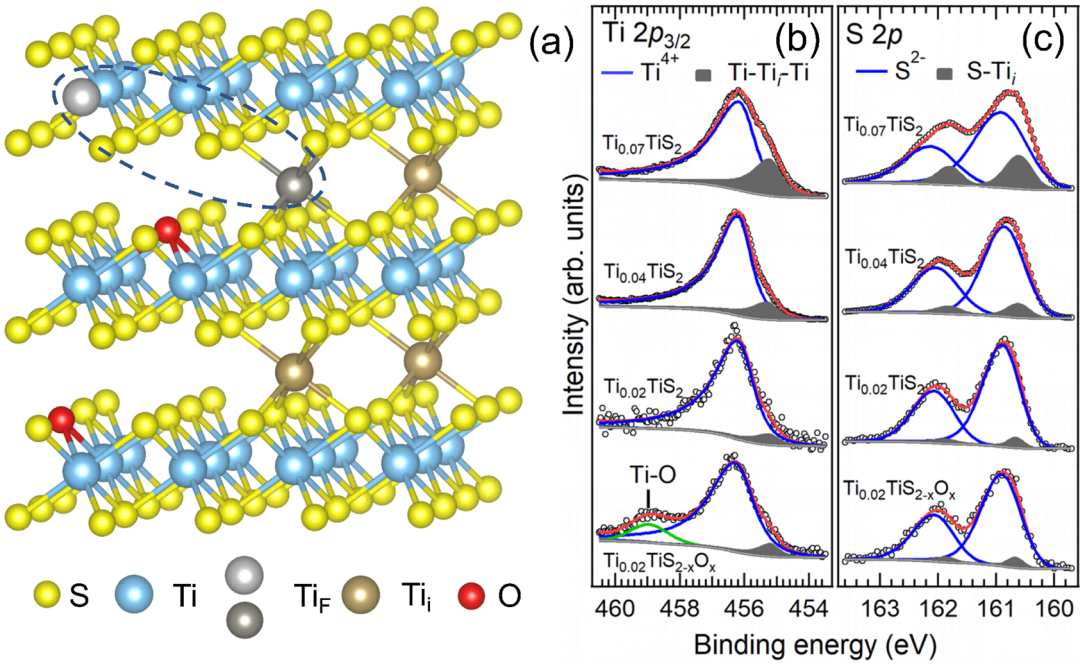

Figure 6. (**a**) Schematic illustration of the crystal structure of 1T-TiS_2 and the corresponding defects. The orange, blue, light-yellow, and red balls represent the S-atoms, Ti-atoms, Ti_i in the vdW gap, and O-atoms, respectively. Ti_F (a vacancy, and an interstitial Ti in vdW gap) is depicted in gray atoms. (**b**) Ti $2p_{3/2}$ and (**c**) S $2p$ core-level PES spectra measured using Al K_α (1486.6 eV). Reproduced from Ref. [23] with permission. Copyright © 2020, AIP Publishing.

3.2. Structural Evolution

In contrast to graphene, which consists of a truly single atomic layer, monolayer TMDs possess a triple-atomic-layers structure in which a transition metal M-plane is sandwiched between two chalcogen X-planes. This X-M-X configuration gives rise to multiple coordination geometries and polymorphic phases. When the two chalcogen layers are aligned in an on-top stacking configuration, the metal atoms adopt trigonal prismatic coordination, forming the 1H phase. This phase is characterized by an out-of-plane AbA stacking sequence, as illustrated in Figure 7a. A relative 60° rotation of the top chalcogen layer with respect to the bottom layer results in an octahedral coordination of metal atoms, giving rise to the 1T phase with an AbC stacking sequence (Figure 7b). In some TMDs systems, the 1T phase is metastable and undergoes a lattice distortion driven by metal-metal bonding, leading to the formation of the distorted 1T'-phase (Figure 7c).

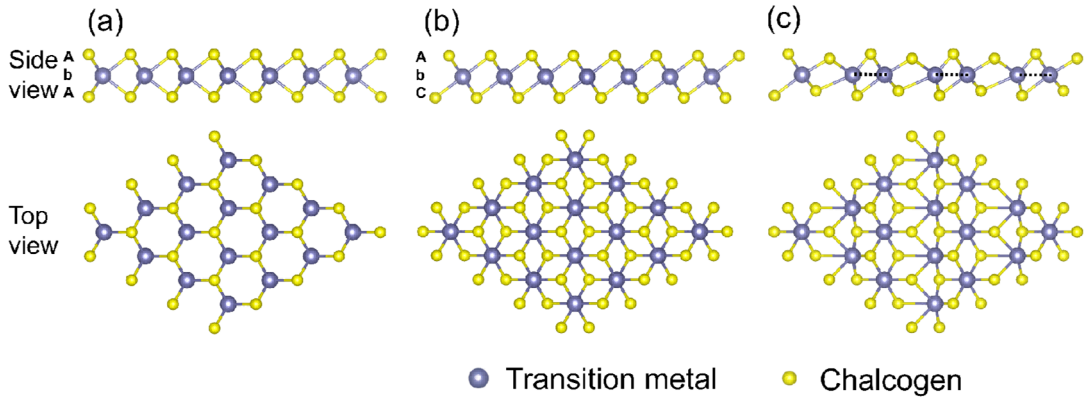

Figure 7. Atomic layer structure of (a) 1H-phase, (b) 1T-phase and (**c**) 1T'-phase of monolayer TMDs.

These structural phases display markedly different physical properties. For instance, 1H-MoS_2 is a semiconductor with ~1.8 eV direct bandgap, suitable for optoelectronic application, whereas 1T'-MoS_2 exhibits metallic behavior with high electrical conductivity [4,24].

The structural phase transitions among these polymorphs can be triggered by various external stimuli, including irradiation, thermal heating, mechanical strain, and pressure. These transitions are primarily governed by intra-layer chalcogen-plane sliding [25], which alters the local coordination environment and thus modifies the electronic structure. Beyond the monolayer limit, vertical stacking of TMD layers introduces additional degree of freedom, particular inter-layer twisting and sliding [26–28]. These structural tunabilities enable precise control over inter-layer coupling, giving rise to emergent phenomena, such as moiré flat bands and sliding ferroelectricity, and establishing new research paradigms, including twistronics and slidetronics [29].

Despite this rich tunability, the reliable identification of different phases and stacking configurations remains challenging due to the subtle structural differences in atomic arrangement and frequent phase coexistence. In this context, spectroscopic techniques sensitive to the local electronic structure are highly desirable. In the following subsections, we present representative examples demonstrating how PES can be employed to resolve (i) intra-layer lattice distortion and the influence of intra-layer sliding, and (ii) intra-layer sliding induced structural phase transition in TMD systems.

3.2.1. Intra-Layer David-Star Distortion and Inter-Layer Sliding in 1T-TaS_2

The CDW state in 1T-TaS_2 can be well resolved by PES. In the nearly-commensurate CDW (NC-CDW) phase associated with David-star distortion, Ta-atoms form characteristic 13-atoms David-star clusters (Figure 8e). Within each cluster, in-plane electron transfer from outer C- and B-Ta-atoms to the central A-Ta-atoms. This unequal charge redistribution gives rise to site-dependent core-hole screening, which further splits the Ta 4*f* doublet to multiple components [30]. As shown in Figure 8g, the Ta 4*f* spectrum of 1T-TaS_2 can therefore be well described by three components corresponding to inequivalent Ta-sites, namely the central (A), nearest-neighbor (B), and next-nearest-neighbor (C) Ta-atoms in the David-star cluster. These components are located at ~22.97 eV (A), ~23.10 eV (B), and ~23.64 eV (C), with an intensity ratio close to 1:6:6, reflecting the intrinsic electron transfer from outer C-/B-Ta to A-Ta atoms.

The intrinsic combination of weak inter-layer vdW interaction and strong intra-layer covalent bonding endows TMDs with pronounced interlayer slipperiness while maintaining in-plane rigidity. As a result, inter-layer

sliding can occur over a wide range of length scales, from bilayers, flakes to bulk crystals [31–35]. Such sliding modifies the inter-layer coupling and induces charge redistribution, which can be sensitively probed by PES.

A representative example is the ladder-like stacking configuration (denoted as LC-TaS_2) formed via a global interlayer translation of ~0.015 nm in 1T-TaS_2 crystals (Figure 8b). Despite the absence of a crystallographic phase transition, this subtle structural modulation leads to measurable electronic reconstruction from 3D band insulator to 2D Mott insulator.

Figure 8g and 8f show the Ta 4*f* and S 2*p* core-level spectra for pristine 1T-TaS_2 and LC-TaS_2. For LC-TaS_2, the binding energies of the B-Ta and C-Ta components remain essentially unchanged, indicating that the CDW order is preserved upon inter-layer sliding. In contrast, the A-Ta component exhibits a discernible shift toward lower binding energy (~0.05 eV), as shown in Figure 8g. This shift signifies an increase in local electron density at the central A-Ta sites. Consistently, the reduced spectral overlap between the A-Ta and B-Ta components slightly modifies the spectral profile (cf, Figure 8h), while the overall intensity ratio (6:6:1) remains conserved.

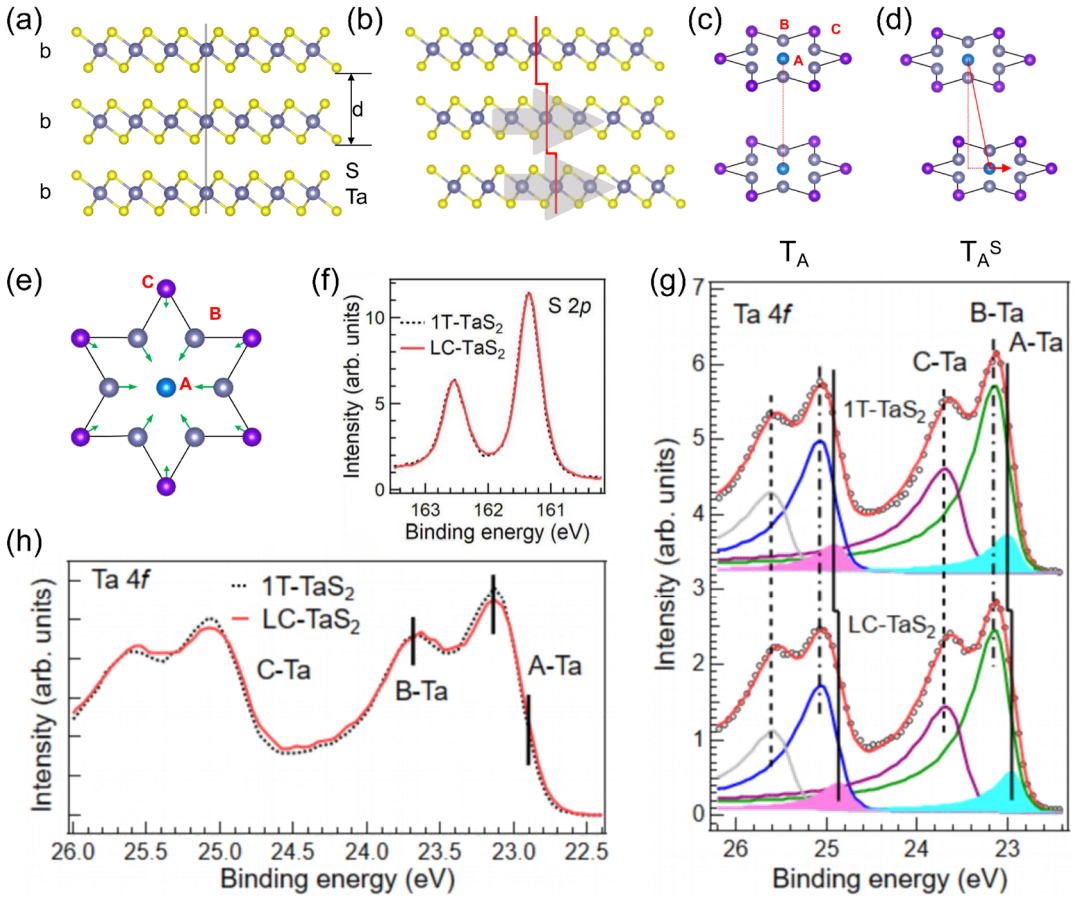

Figure 8. Schematic side view of (**a**) 1T-TaS_2 crystals and (**b**) the laddering stack structure in LC-TaS_2 crystals). Illustration of (**c**) the David-stars T_A stacking in 1T-TaS_2 and LC-TaS_2. (**d**) the T^S_A stacking. (**e**) David-star cluster. (**g**) S 2*p* and (**f**) Ta 4*f* core-level spectra with corresponding fitting curves measured at room temperature. (**g**,**h**) Comparison of Ta 4*f* core-level spectra of pristine 1T-TaS_2 and LC-TaS_2. Reproduced from Ref. [36] with permission. Copyright © 2024, Nature.

Alternative interpretations, such as the formation of the 1H phase or the presence of Ta^{3+} species associated with S-vacancy defects, can be excluded. First, the S 2*p* spectrum of LC-TaS_2 remains nearly identical to that of pristine 1T-TaS_2, with no additional feature near ~160.8 eV, which would otherwise indicate the emergence of the 1H phase (as discussed later). Second, the Ta:S intensity ratio remains nearly constant, confirming that the chemical stoichiometry is preserved and ruling out defect-induced effects.

From a physical standpoint, the observed site-selective binding energy shift can be attributed to inter-layer decoupling induced by the ladder-like sliding configuration. The reduced inter-layer overlap suppresses the dimerization of adjacent David-star clusters, which would otherwise lead to an even-electron band-insulating state. Instead, the system retains an odd number of electrons per David-star unit, preserving the Mott-insulating character. This enhanced electronic localization at the central A-sites strengthens the screening of the photon-induced core-hole, stabilizing a well-screened final state and resulting in the observed low-binding-energy shift.

Overall, this example demonstrates that PES can resolve both intra-layer charge transfer induced and inter-layer sliding induced electronic reconstruction through subtle, site-selective spectral shifts, even in the absence of new spectral components. In particular, intra-layer CDW order manifests as multiple well-defined components due to site-dependent screening, whereas inter-layer sliding primarily induces fine binding energy shifts without generating new spectral features.

3.2.21. 1T-to-1H Transition [37]

A representative example demonstrating the capability of PES in resolving structural phase transitions is the surface-limited 1T-to-1H transformation in TaS_2 induced by moderate thermal annealing, as illustrated in Figure 9a. This transition can be clearly identified by comparing the S 2*p* and Ta 4*f* core-level spectra of annealed sample with these of the as-grown 1T-TaS_2 reference, as shows in Figure 9b,c.

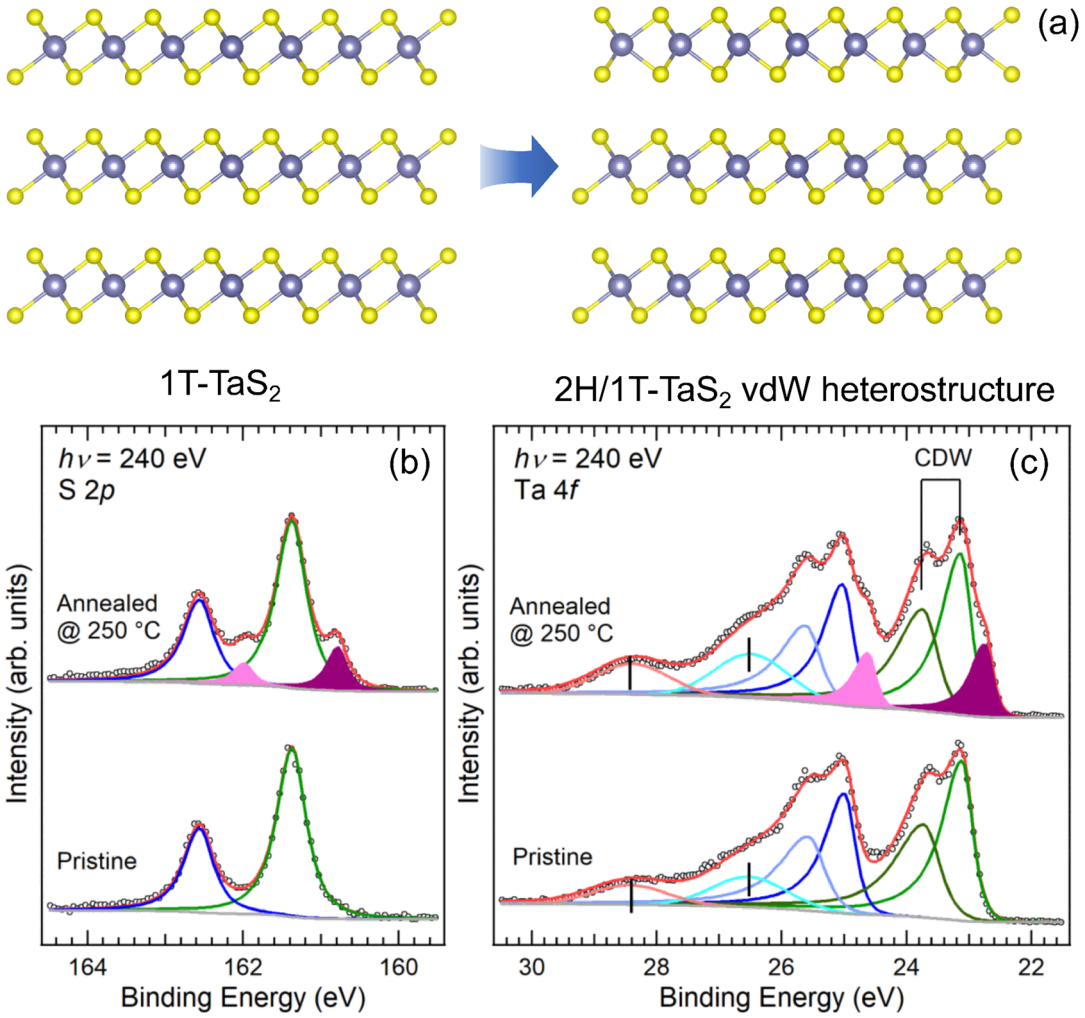

Figure 9. (**a**) The surface limited 1T-to-1H transformation in TaS_2. (**b**) The S 2*p* and (**c**) Ta 4*f* core-levels for pristine 1T-TaS_2 and sample annealed at 250 °C. Both samples are transferred to PES chamber after several minutes of air expose. Reproduced from Ref. [37] with permission. Copyright © 2018, American Chemical Society.

In pristine 1T-TaS_2, the S 2*p* spectrum exhibits a well-resolved doublet with the dominant S $2p_{3/2}$ peak located at ~161.4 eV. Upon annealing, an additional doublet (purple and pink shaded peaks) appears at the lower binding energies, with the S $2p_{3/2}$ peak at ~160.8 eV. The energy difference of ~0.6 eV is consistent with the reported value between the 1T- and 2H-TaS_2 crystals[38], providing direct spectroscopic evidence of phase transformation.

Further insight is obtained from the Ta 4*f* spectra (Figure 9c). For simplicity, the Ta 4*f* spectrum is described by two main components: a dominant feature at ~23.1 eV representing one central A-Ta-atoms and six nearest-neighbor B-Ta-atoms (Figure 9), and a higher binding energy component at ~23.7 eV attributed to the six next-nearest-neighbor C-Ta-atoms. After formation of 1H-TaS_2, a new Ta 4*f* doublet emerges at lower binding energies (~22.8 eV and ~24.7 eV). This assignment is supported by two key observations: (i) the binding energy difference

matches well with literature values for the 1H-TaS_2 [38–40], and (ii) the Ta:S ratio determined from integrating spectral weight of 1T-phase and 1H-phase consistent with the stoichiometric value of 1:2. This confirms the intrinsic nature of the phase transition rather than defect-induced chemical variation.

The lower binding energy of the 1H-TaS_2 can be understood in terms of enhance the core-hole screening. Due to its metallic character, 1H-TaS_2 provides a higher density of mobile carriers, enabling more efficient screening of the core-hole created during the photoemission process. This stabilizes a well-screened final state and thereby shifts the measured binding energy to lower values. This interpretation is consistent with general trends observed in TMD systems. For example, the metallic 1T'-MoS_2 exhibit lower binding energy components in both Mo 3*d* and S 2*p* spectra compared to the semiconducting 1H-MoS_2 (Figure 10), reflecting stronger screening. The nearly constant binding energy for coexisting phases indicates negligible charge transfer between them.

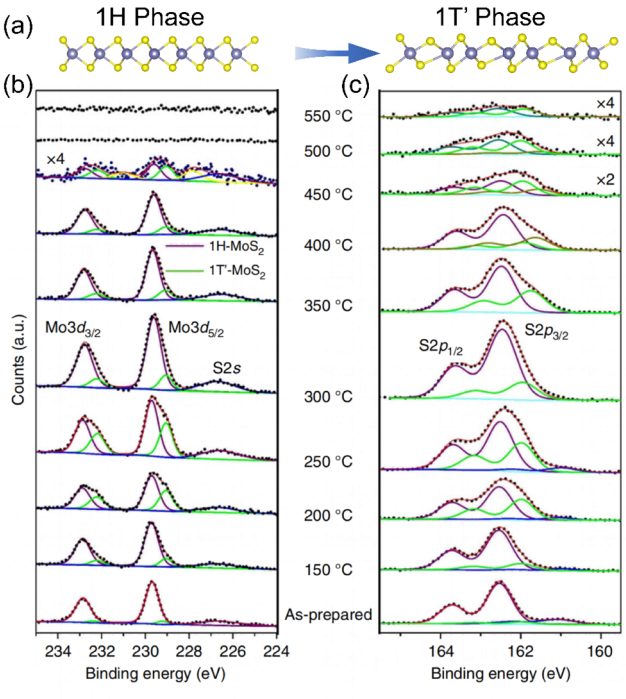

Figure 10. (**a**) Temperature dependence of PES spectra associated with 1H-to-1T' transformation in MoS_2. (**b**) Mo 3*d* and (**c**) S 2*p* spectra for MoS_2/Au after annealing at respective temperatures. Reproduced from Ref. [41] with permission. Copyright © 2017, Nature.

Overall, both examples demonstrate that PES can reliably identify structural phase transformation even when the chemical state remains unchanged. The emergence of new spectral components and the consistency between multiple core-levels together provide a robust and quantitative framework for distinguishing structural phase transformation. Such capabilities are particularly important for TMD systems under external stimuli, where phase coexistence and spatially confined transformations are frequently encountered.

4. Conclusions and Outlook

In this review, we have demonstrated that PES provides a powerful and unified framework for resolving structural characteristics and structural evolution in layered TMDs. Unlike conventional techniques that mainly probe composition or long-range order, PES directly accesses the local electronic structure and chemical environment, enabling the identification of subtle yet critical structural variations.

A central insight is that structural variations in TMDs can be systematically decoded via the *electronic fingerprints* captured by PES. Different structural degrees of freedom give rise to distinct and quantifiable spectroscopic signatures governed by initial-state chemical shifts and final-state core-hole screening. A self-consistent analysis of these spectroscopic responses enables PES to disentangle defect formation, lattice distortion, stacking modulation and structural phase transition within a unified framework.

Despite these strengths, several limitations remain. PES typically requires ultrahigh vacuum conditions, limiting its applicability to realistic or operando environments. Its spatial resolution is generally restricted to the microscale, hindering direct observation of nanoscale defects and phase coexistence.

Another important direction is the correlative use of PES with complementary structural and vibrational characterization techniques. While PES directly probes the local electronic structure, chemical environment, and core-hole screening response, techniques such as STEM and Raman spectroscopy provide structural information from different perspectives. STEM can directly visualize atomic defects, local lattice distortion, stacking configurations, and phase boundaries at the nanoscale, whereas Raman spectroscopy is sensitive to phonon modes, strain, layer number, interlayer coupling, and phase-dependent lattice symmetry. Combining PES with STEM and Raman spectroscopy can therefore establish a more complete structure-spectroscopy-property correlation. For example, STEM can identify the atomic origin of defects or phase coexistence, Raman spectroscopy can track lattice symmetry and vibrational fingerprints, and PES can determine the corresponding chemical shifts, charge redistribution, and screening channels. Such multimodal characterization will be particularly valuable for TMD systems with subtle structural disorder, mixed phases, local intercalation, or spatially inhomogeneous electronic reconstruction.

Looking forward, continued methodological advances are expected to significantly expand the capability of PES. The development of ambient-pressure and operando PES will enable investigations under realistic working conditions. Improvements in spatial resolution through nano-resolved and imaging PES will allow direct mapping of structural heterogeneity at the nanoscale. In addition, the integration of machine learning and data-driven approaches will enable automated and high-throughput spectral analysis, further enhancing the interpretability of complex spectral features.

Author Contributions

H.L. drafted the manuscript. L.C. and H.X. designed the structure of the review, reviewed and edited the manuscript. All authors have read and agreed to the published version of the manuscript

Funding

This research received no external funding.

Institutional Review Board Statement

Not applicable.

Informed Consent Statement

Not applicable.

Data Availability Statement

No new data were generated or analyzed in this review. All figures and data discussed in this article are derived from previously published literature, and the original sources are cited in the corresponding figure captions and/or main text.

Conflicts of Interest

The authors declare no conflict of interest.

Use of AI and AI-Assisted Technologies

During the preparation of this work, the authors used ChatGPT for language polishing only. After using this tool, the authors reviewed and edited the content as needed and take full responsibility for the content of the published article."

References

1. Novoselov, K.S.; Geim, A.K.; Morozov, S.V.; et al. Electric field effect in atomically thin carbon films. *Science* **2004**, *306*, 666–669.
2. Chowdhury, T.; Sadler, E.C.; Kempa, T.J. Progress and prospects in transition-metal dichalcogenide research beyond 2D. *Chem. Rev.* **2020**, *120*, 12563–12591.
3. Zhai, W.; Li, Z.; Wang, Y.; et al. Phase engineering of nanomaterials: Transition metal dichalcogenides. *Chem. Rev.* **2024**, *124*, 4479–4539.
4. Wang, Q.H.; Kalantar-Zadeh, K.; Kis, A.; et al. Electronics and optoelectronics of two-dimensional transition metal dichalcogenides. *Nat. Nanotechnol.* **2012**, *7*, 699–712.

5. Chhowalla, M.; Shin, H.S.; Eda, G.; et al. The chemistry of two-dimensional layered transition metal dichalcogenide nanosheets. *Nat. Chem.* **2013**, *5*, 263–275.
6. Li, H.; Li, Y.; Aljarb, A.; et al. Epitaxial growth of two-dimensional layered transition-metal dichalcogenides: Growth mechanism, controllability, and scalability. *Chem. Rev.* **2017**, *118*, 6134–6150.
7. Manzeli, S.; Ovchinnikov, D.; Pasquier, D.; et al. 2D transition metal dichalcogenides. *Nat. Rev. Mater.* **2017**, *2*, 17033.
8. Hu, Z.; Wu, Z.; Han, C.; et al. Two-dimensional transition metal dichalcogenides: Interface and defect engineering. *Chem. Soc. Rev.* **2018**, *47*, 3100–3128.
9. Addou, R.; Wallace, R.M. Using photoelectron spectroscopy in the integration of 2D materials for advanced devices. *J. Electron Spectrosc. Relat. Phenom.* **2019**, *231*, 94–103.
10. Zhang, X.; Qiao, X.-F.; Shi, W.; et al. Phonon and Raman scattering of two-dimensional transition metal dichalcogenides from monolayer, multilayer to bulk material. *Chem. Soc. Rev.* **2015**, *44*, 2757–2785.
11. Zeng, L.; Olsson, E. Control of electrically and optically active structural disorder in 2D transition metal dichalcogenides. *npj 2D Mater. Appl.* **2026**, *10*, 8.
12. Hu, J.; Huang, C.; Liu, L.; et al. Defect-Mediated Phase Transitions and Structural Dynamics in Single-Layer VSe_2. *ACS Appl. Mater. Interfaces* **2025**, *17*, 47781–47789.
13. Liang, Z.; Zhang, J.; Hua, C.; et al. Ferroelectric manipulation and enhancement of Rashba spin splitting in van der Waals heterostructures. *Phys. Rev. B* **2024**, *110*, 085110.
14. Lin, Z.; Carvalho, B.R.; Kahn, E.; et al. Defect engineering of two-dimensional transition metal dichalcogenides. *2D Mater.* **2016**, *3*, 022002.
15. Bussolotti, F.; Kawai, H.; Maddumapatabandi, T.D.; et al. Role of S-vacancy concentration in air oxidation of WS_2 single crystals. *ACS Nano* **2024**, *18*, 8706–8717.
16. Zhang, P.; Xue, M.; Chen, C.; et al. Mechanism regulating self-intercalation in layered materials. *Nano Lett.* **2023**, *23*, 3623–3629.
17. Zhao, X.; Song, P.; Wang, C.; et al. Engineering covalently bonded 2D layered materials by self-intercalation. *Nature* **2020**, *581*, 171–177.
18. Wu, S.; Tian, W.; Li, R.; et al. Self-intercalated 6R-TaS_2 with reduced symmetry for room temperature nonlinear Hall effect. *Matter* **2025**, *8*, 102153.
19. Han, Z.; Han, X.; Wu, S.; et al. Phase and composition engineering of self-intercalated 2D metallic tantalum sulfide for second-harmonic generation. *ACS Nano* **2024**, *18*, 6256–6265.
20. Wang, H.; Zhang, J.; Shen, C.; et al. Direct visualization of stacking-selective self-intercalation in epitaxial $Nb_{1+x}Se_2$ films. *Nat. Commun.* **2024**, *15*, 2541.
21. Hong, J.; Peela, B.; Georgescu, A.B.; et al. Influence of chromium intercalation in self-intercalated van der Waals magnets $Cr_{1+\delta}Te_2$. *Phys. Rev. Mater.* **2025**, *9*, 094414.
22. Sung, H.Y.; Wang, C.H.; Lee, M.P.; et al. Titanium Self-Intercalation in Titanium Diselenide Devices: Insights from In Situ Transmission Electron Microscopy. *Adv. Mater.* **2025**, *37*, 2418557.
23. Chen, K.; Song, M.; Sun, Y.-Y.; et al. Defects controlled doping and electrical transport in TiS_2 single crystals. *Appl. Phys. Lett.* **2020**, *116*, 121901.
24. Mak, K.F.; Lee, C.; Hone, J.; et al. Atomically thin MoS_2: A new direct-gap semiconductor. *Phys. Rev. Lett.* **2010**, *105*, 136805.
25. Lin, Y.-C.; Dumcenco, D.O.; Huang, Y.-S.; et al. Atomic mechanism of the semiconducting-to-metallic phase transition in single-layered MoS_2. *Nat. Nanotechnol.* **2014**, *9*, 391–396.
26. Cao, Y.; Fatemi, V.; Demir, A.; et al. Correlated insulator behaviour at half-filling in magic-angle graphene superlattices. *Nature* **2018**, *556*, 80–84.
27. Cao, Y.; Fatemi, V.; Fang, S.; et al. Unconventional superconductivity in magic-angle graphene superlattices. *Nature* **2018**, *556*, 43–50.
28. Vizner Stern, M.; Waschitz, Y.; Cao, W.; et al. Interfacial ferroelectricity by van der Waals sliding. *Science* **2021**, *372*, 1462–1466.
29. Han, X.; Zhao, X. Stackingtronics: Programmable Interlayer Sliding in 2D Materials. *Nano Lett.* **2025**, *25*, 16955–16962.
30. Hughes, H.P.; Starnberg, H. *Electron Spectroscopies Applied to Low-Dimensional Structures*; Springer Dordrecht: Dordrecht, The Netherlands, 2001.
31. Fox, C.; Mao, Y.; Zhang, X.; et al. Stacking order engineering of two-dimensional materials and device applications. *Chem. Rev.* **2023**, *124*, 1862–1898.
32. Yasuda, K.; Wang, X.; Watanabe, K.; et al. Stacking-engineered ferroelectricity in bilayer boron nitride. *Science* **2021**, *372*, 1458–1462.
33. Yasuda, K.; Zalys-Geller, E.; Wang, X.; et al. Ultrafast high-endurance memory based on sliding ferroelectrics. *Science* **2024**, *385*, 53–56.

34. Wang, X.; Yasuda, K.; Zhang, Y.; et al. Interfacial ferroelectricity in rhombohedral-stacked bilayer transition metal dichalcogenides. *Nat. Nanotechnol.* **2022**, *17*, 367–371.
35. Bian, R.; He, R.; Pan, E.; et al. W. Developing fatigue-resistant ferroelectrics using interlayer sliding switching. *Science* **2024**, *385*, 57–62.
36. Wang, Y.; Li, Z.; Luo, X.; et al. Dualistic insulator states in 1T-TaS_2 crystals. *Nat. Commun.* **2024**, *15*, 3425.
37. Wang, Z.; Sun, Y.-Y.; Abdelwahab, I.; et al. Surface-limited superconducting phase transition on 1T-TaS_2. *ACS Nano* **2018**, *12*, 12619–12628.
38. Tison, Y.; Martinez, H.; Baraille, I.; et al. X-ray photoelectron spectroscopy and scanning tunneling microscopy investigations of the solid solutions $Ti_xTa_{1-x}S_2$ ($0 \leq x \leq 1$). *Surf. Sci.* **2004**, *563*, 83–98.
39. Crawack, H.; Pettenkofer, C. Calculation and XPS measurements of the Ta 4f CDW splitting in Cu, Cs and Li intercalation phases of 1T-TaX_2 (X = S, Se). *Solid State Commun.* **2001**, *118*, 325–332.
40. Luxa, J.; Mazánek, V.; Pumera, M.; et al. 2H→1T phase engineering of layered tantalum disulfides in electrocatalysis: Oxygen reduction reaction. *Chem. Eur. J.* **2017**, *23*, 8082–8091.
41. Yin, X.; Wang, Q.; Cao, L.; et al. Tunable inverted gap in monolayer quasi-metallic MoS_2 induced by strong charge-lattice coupling. *Nat. Commun.* **2017**, *8*, 486.